Modeling and Analysis of a Novel Two-Axis Rotary Electromagnetic Actuator for Fast Steering Mirror

Yongjun Long, Chunlei Wang, Xin Dai, Xiaohui Wei, and Shigang Wang*

The State Key Laboratory of Mechanical System and Vibration, School of Mechanical Engineering, Shanghai Jiao Tong University, 800 Dongchuan Road, Shanghai 200240, China

This paper focuses on the modeling and analysis a novel two-axis rotary normal-stress electromagnetic actuator with compact structure for fast steering mirror (FSM). The actuator has high force density similar to a solenoid, but its torque output is nearly a linear function of both its driving current and rotation angle, showing that the actuator is ideal for FSM. In addition, the actuator is designed with a new cross topology armature and no additional axial force is generated when the actuator works. With flux leakage being involved in the actuator modeling properly, an accurate analytical model of the actuator, which shows the actuator's linear characteristics, is obtained via the commonly used equivalent magnetic circuit method. Finally, numerical simulation is presented to validate the analytical actuator model. It is shown that the analytical results are in a good agreement with the simulation results.

Keywords : fast steering mirror, electromagnetic actuator, normal stress, linear characteristics, symmetric electromagnetic structure.

1. Introduction

Fast steering mirror (FSM) is widely used in adaptive optical system to adjust a beam to a desired position with high pointing accuracy and high response speed. The performance of a FSM is greatly affected by its actuator. In general, FSMs are driven by voice coil actuators [1-4] or piezoelectric actuators [5, 6]. Voice coil actuators allow long actuation strokes with low input power requirements. However, their peak force outputs are limited by the heat produced in the coil windings. Conversely, piezoelectric actuators allow high accelerations and quick responses accompanied by short actuation strokes and high voltage requirements. Hence, the FSMs using voice coil actuators achieve wider scanning areas but lower bandwidths whereas the piezoelectrically driven FSMs allow higher bandwidths but narrower scanning areas. An actuator combing the advantages of both voice coil actuators and piezoelectric actuators should be ideal for FSM.

In Ref. [7], Lu developed a normal-stress solenoid-type electromagnetic actuator by using magnetic-flux-biased

method. By involving bias flux and designing proper electromagnetic configuration, the actuator has high force density similar to a solenoid, but its force output is a linear function of both driving current and armature displacement, thereby simplifying control algorithm design. So far, magnetic-flux-biased normal-stress actuators have been successfully employed in fast tool servos [7-9] and nanopositioner [10]. In fact, the basic electromagnetic structure of flux-biased actuator is not new and has been used in servovalve since 1950s [11].

The effective stroke of the actuator in Ref. [7] is between the strokes of a piezoelectric actuator and a voice coil actuator, indicating that the actuator is ideal for FSM by combing the actuator's force output characteristics. Based on the work of Ref. [7], Kluk *et al.* designed two fast steering mirrors named the AFSM and sAFSM [12], respectively. The two FSMs, however, have some drawbacks. In the AFSM, the permanent magnets (PMs) used to generate bias fluxes are located inside the cores, hence enlarging the size of the AFSM. The sAFSM achieves a far more compact structure than the AFSM by introducing a ring armature topology. However, as the sAFSM is vertically asymmetric, we note that an additional axial force which varies with the sAFSM driving current is generated on the armature when the sAFSM works. Hence,

*Corresponding author: Tel: +86-21-34204496
Fax: +86-21-34204496, e-mail: wangshigang@sjtu.edu.cn

resonance occurs when the frequency of the sAFSM driving current matches the natural frequency of the structural mode moving along the vertical direction. As a result, the beam path length changes significantly and the sAFSM may be damaged. As there are only two PMs used to generate bias flux for one air gap in the sAFSM, big PMs are needed if a high bias flux density is wanted, thereby enlarging the sAFSM size. Besides, flux leakage was not involved in the magnetic analysis when modeling the actuators in Ref. [12]. Hence, a sAFSM actuator model with low accuracy was obtained.

In this paper, a novel flux-biased rotary electromagnetic actuator that overcomes the drawbacks of the actuators in the AFSM and sAFSM is designed to drive our FSM. Besides, a cross armature topology is introduced to decrease the actuator's moment of inertia about the working axis and thus a higher bandwidth of our FSM can be achieved. The actuator is analyzed and modeled carefully, and an accurate analytical model of the actuator is finally obtained. Both the concept design and obtained analytical actuator model are validated by finite element simulations.

2. Concept Design and Operating Principle

First, the basic layout and operating principle of our FSM is introduced in this section. Then, the concept design of the actuator in our FSM is presented. Apart from overcoming the drawbacks of the actuators in the AFSM and sAFSM, the actuator in this paper has some other advantages which can improve the performance of our FSM. Finally, the basic operating principle of the actuator is introduced in an intuitive way at the end of this section.

2.1. Structure and Operating Principle of the FSM

The structure overview of our FSM is displayed in Fig. 1. The FSM is mainly composed of the mirror, flexure support system, electromagnetic actuator, and angle detection system. The mirror is placed in the center and mounted on the mirror holder. The flexure support system, which consists of the flexible diaphragm and axial flexure, offers restoring torque against actuating torque to yield angle control. The flexure support system allows θ_X and θ_Y rotation whereas restrains X, Y, and Z translation and θ_Z rotation. The electromagnetic actuator is mainly composed of four identical electromagnetic units and an armature. Utilizing the torques generated by the electromagnetic actuator, the FSM can produce two rotary motions, θ_X and θ_Y, simultaneously. The angle detection system which is mainly composed of four displacement sensors detects the steering angle of the mirror in real time to yield steering angle closed-loop control.

2.2. Concept Design of the Electromagnetic Actuator in the FSM

To avoid the drawbacks of the AFSM and sAFMS, a new flux-biased electromagnetic actuator with vertically symmetric electromagnetic structure and new armature topology is designed in this paper. This new electromagnetic actuator works on normal stress and hence has high force density. By introducing bias magnetic flux into the actuator's magnetic circuit, the actuator has essentially linear characteristics. The schematic diagram of the actuator is illustrated in Fig. 2. As Fig. 2 shows, each PM used to generate bias flux in the air gaps is located between two cores in the circumferential direction, leading to a compact structure of the FSM. Differing from the placement of the PMs only at the bottoms of the cores in the sAFSM, both the tops and bottoms of the cores are placed
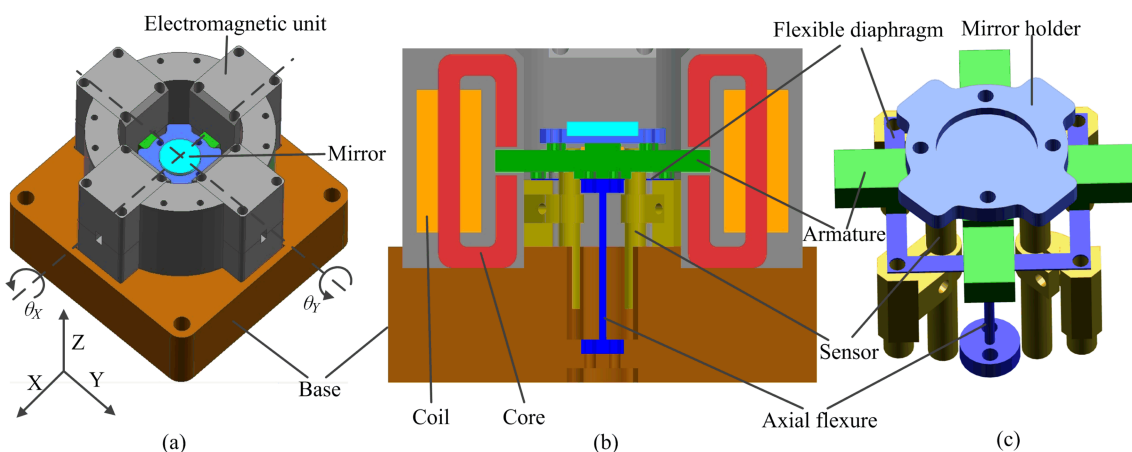

Fig. 1. (Color online) Structure overview of our FSM. (a) Three-dimensional CAD shape of the FSM, (b) cross-sectional view of the FSM, (c) flexure support system of the FSM.
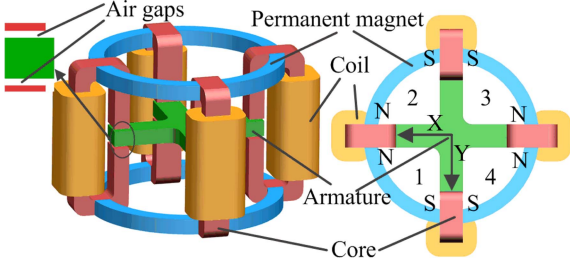
Fig. 2. (Color online) Schematic diagram of the actuator in this paper.

Fig. 3. Cross topology armature and its corresponding ring topology armature.

with PMs in our actuator. We will refer to this type of arrangement as "top-bottom" arrangement in the following analysis. The "top-bottom" arrangement of the PMs is not new and has been presented in Ref. [13]. However, Ref. [13] presented this arrangement only in its appendix as a potential replacement for the arrangement of the PMs in the sAFSM, without discussing this new electromagnetic topology in detail. Besides, as the core is vertically asymmetric, the sAFSM will still suffer from the additional axial force problem even though the "top-bottom" arrangement is used. As Fig. 2 shows, the core in our actuator is vertically symmetric. Hence, our actuator is vertically symmetric by combing the "top-bottom" arrangement of the PMs. As a result, no additional axial force will be generated on the armature when our FSM works. Benefiting from the "top-bottom" arrangement of the PMs, it is capable of achieving a high bias flux density in each air gap without the need of big PMs.

Except the armature, all the components in Fig. 2 are stationary. To decrease power consumption and the heat generated eddy current, the core and the armature are laminated with nickel-iron alloy which is a kind of soft magnetic material with high magnetic permeability. Differing from the ring armature used in the sAFSM [12], the actuator is with a new cross topology armature. In the following analysis, we will show that the cross topology armature has smaller moment of inertia than the ring topology armature in the sAFSM if they can conduct the same maximum amount of magnetic flux. Thereby, a higher acceleration and bandwidth of our FSM can be achieved. Fig. 3 shows a cross armature and its corresponding ring armature. The moments of inertia of the cross and ring armatures about the dotted centerline can be calculated as

$$J_C = \frac{\rho D_O L_C t_C \left(D_O^2 + 2t_C^2 + L_C^2\right)}{12} - \frac{\rho L_C^2 t_C \left(L_C^2 + t_C^2\right)}{12} \tag{1}$$

$$J_R = \frac{\rho \pi t_R \left(D_O^2 - D_I^2\right)\left(0.75D_O^2 + 0.75D_I^2 + t_R^2\right)}{48} \tag{2}$$

where J_C, J_R, and ρ denote the moment of inertia of the
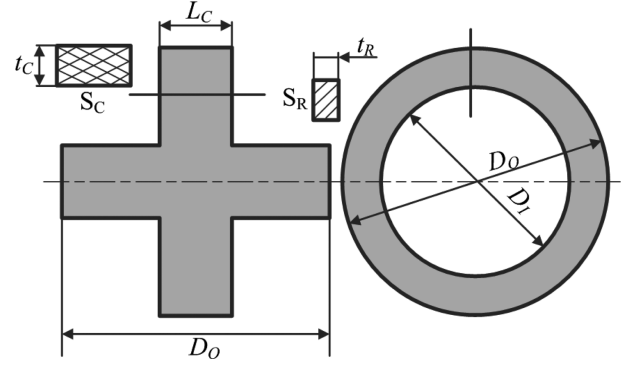
cross armature, the moment of inertia of the ring armature, and the mass density of the two armatures.

By viewing Fig. 2 and Fig. 3, it is easy to obtain that the cross sectional area of the cross armature, S_C, is twice that of the corresponding ring armature, S_R. Hence, the following result is obtained

$$t_R \left(D_0 - D_I\right) = L_C t_C \tag{3}$$

$$\frac{J_C}{J_R} \approx \frac{16D_O \left(D_O^2 + 2t_C^2 + L_C^2\right)}{3\pi \left(D_O + D_I\right)\left(D_O^2 + D_I^2 + 4t_R^2/3\right)} \tag{4}$$

In general, the designed results of the cross and ring armatures meet the following two conditions

$$\frac{16D_O}{3\pi \left(D_O + D_I\right)} \approx 1 \tag{5}$$

$$\frac{\left(D_O^2 + 2t_C^2 + L_C^2\right)}{\left(D_O^2 + D_I^2 + 4t_R^2/3\right)} < 1 \tag{6}$$

Hence the ratio of J_C to J_R is always smaller than one, indicating that the cross topology armature always has smaller moment of inertia than the ring topology armature for most designs.

2.3. Motion Generation of the Electromagnetic Actuator

Due to the symmetry of the actuator, the analysis of the steering motion θ_Y is the same as that of the steering motion θ_X. In the following analysis, only the steering motion θ_X is concerned. Fig. 4 illustrates the coil and PM fluxes that control the steering motion θ_X. The PM flux (bias flux) is generated by the PMs. The coil flux is generated by the excitation coil windings and varies with the driving current. If the directions of the two currents that control the steering motion θ_X are the same as those shown in Fig. 4, the fluxes in the right upper and left lower air gaps are enhanced while those in the right lower and left upper air gaps are reduced simultaneously. Con-
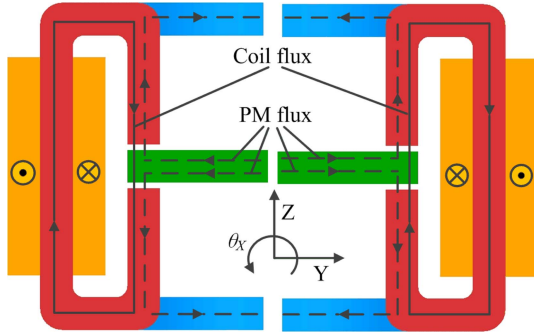
Fig. 4. (Color online) Coil and PM fluxes that control the steering motion θ_X.

sequently, a torque pointing to the positive X-direction is generated on the armature and a positive steering angle θ_X is then produced. Reversing the directions of both the two currents will reverse the torque's direction. But if only one current changes its direction, a net force will be generated on the armature.

3. Analytical Model of the Actuator

In the previous section, the motion generating principle of our FSM actuator is described in an intuitive way. In this section, the actuator's operating principle is presented through analyzing the magnetic circuit of the actuator in detail. The commonly used equivalent magnetic circuit method is employed to the magnetic analysis and actuating torque calculation of the actuator. Both the PM flux leakage and coil flux leakage are involved in the modeling of the actuator through 3D finite element simulations which are carried out by using Maxwell 3-D electromagnetic FEM software package. As the actuator is symmetric, only the magnetic analysis related to the steering motion θ_X is introduced in detail in this section.

3.1. Magnetic Circuit Analysis

Fig. 5 shows the ideal equivalent magnetic circuit model of the actuator without considering flux leakage and fringing loss. The reluctances of the cores and armature are assumed to be zero for the high magnetic permeability of their materials. In the magnetic circuit, each PM is modeled as a magnetomotive force (MMF) source with internal reluctance. For example, R_{1U} and Ψ_{1U} respectively denote the reluctance and MMF of the upper PM in the area of "1" (refer to Fig. 2), R_{1L} and Ψ_{1L} respectively denote the reluctance and MMF of the lower PM in the area of "1", and so on. To achieve electromagnetic symmetry, all the permanent magnets used to generate bias fluxes are identical. Using L_{PM}, A_{PM}, and B_r to respectively represent the identical PM length, cross sectional

area and remanence, we obtain the identical MMF and reluctance of the PMs as

$$\Psi_{PM} = \frac{B_r L_{PM}}{\mu_0} \tag{7}$$

$$R_{PM} = \frac{L_{PM}}{\mu_0 A_{PM}} \tag{8}$$

where Ψ_{PM} and R_{PM} represent the identical PM MMF and PM reluctance, respectively.

Each excitation coil is modeled as a coil MMF. For example, Ψ_{+Y} indicates the MMF of the coil in the positive Y-direction, Ψ_{-Y} indicates the MMF of the coil in the negative Y-direction, and so on. In our design, the two coils that control the same steering motion are physically wired together, trying to eliminate additional force. Therefore, Ψ_{+Y} is equal to Ψ_{-Y} and can be given by

$$\Psi_{+Y} = \Psi_{-Y} = NI_Y \tag{9}$$

where N is the number of coil turns and I_Y is the identical driving current in the "+Y" and "−Y" coils. The positive direction of the driving current I_Y is the same as that shown in Fig. 4.

Each air gap is modeled as a reluctance. For example, R_{+YU} is the reluctance of the upper air gap in the positive Y-direction, R_{+YL} is reluctance of the lower air gap in the positive Y-direction, and so on. Using L_0 to denote the air gap length when the armature is centered and making use of small angle approximation, we obtain R_{+YU} and R_{+YL} as

$$R_{+YU} = \frac{L_0 - \theta_X r}{\mu_0 A_g} \tag{10}$$

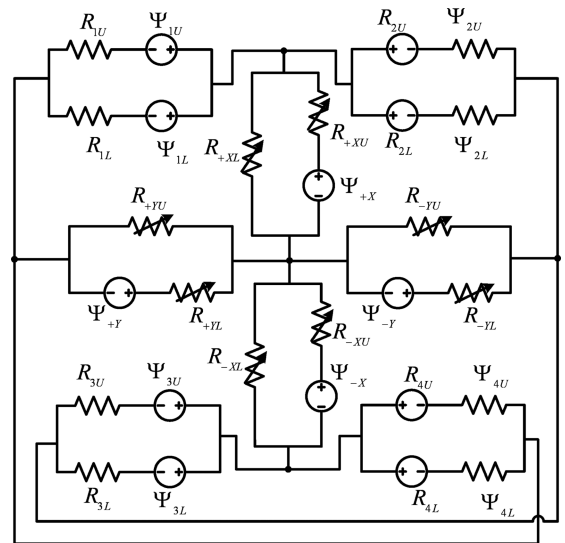$$R_{+YL} = \frac{L_0 + \theta_X r}{\mu_0 A_g} \tag{11}$$

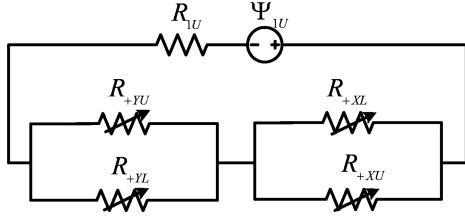**Fig. 5.** Equivalent magnetic circuit of the actuator.

Fig. 6. Equivalent magnetic circuit associated with the "1U" PM.

where r is the effective radius of rotation and A_g is the pole area of the air gaps.

Keep in mind that the reluctance of the PMs is far larger than that of the air gaps. Hence, we can assume that the bias flux generated by a PM does not flow into the other PMs and the coil fluxes prefer to pass through the cores, armature and air gaps, without flowing into any PMs. Hence, the equivalent magnetic circuit associated with the "1U" PM and the equivalent coil flux magnetic circuit can be simplified as Fig. 6 shows and Fig. 7 shows, respectively. According to the actuator's symmetry, the equivalent magnetic circuits associated with the other PMs have the similar form as shown by Fig. 6.

By solving the equivalent magnetic circuit model shown by Fig. 6, the PM fluxes that are generated by the "1U" PM and flow through the "+Y" upper and lower air gaps are determined as follows

$$\Phi_{+YU}^{1U} = \frac{\Psi_{PM}}{R_{+YU} \, / / \, R_{+YL} + R_{+XU} \, / / \, R_{+XL} + R_{PM}} \cdot \frac{R_{+YL}}{R_{+YL} + R_{+YU}} \quad (12)$$

$$\Phi_{+YL}^{1U} = \frac{\Psi_{PM}}{R_{+YU} \, / / \, R_{+YL} + R_{+XU} \, / / \, R_{+XL} + R_{PM}} \cdot \frac{R_{+YU}}{R_{+YL} + R_{+YU}} \quad (13)$$

Setting the armature at center position ($\theta_X = 0$ and $\theta_Y = 0$) gives the maximum value of $R_{+YU} \, / / \, R_{+YL} + R_{+XU} \, / / \, R_{+XL}$, and the ratio of this maximum value to R_{PM} is
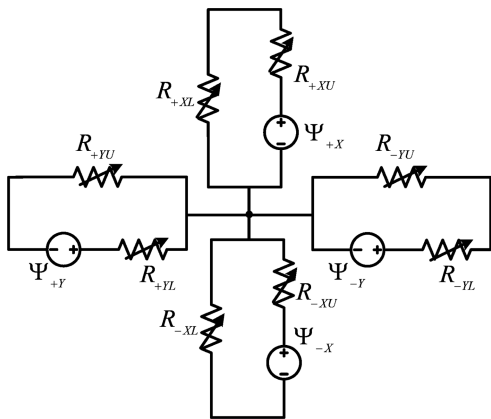

Fig. 7. Equivalent coil flux magnetic circuit.

$$\frac{\max \left(R_{+YU} \, / / \, R_{+YL} + R_{+XU} \, / / \, R_{+XL} \right)}{R_{PM}} = \frac{A_{PM}}{A_g} \cdot \frac{L_0}{L_{PM}} \quad (14)$$

In most applications, A_{PM} is approximately equal to A_g and L_0 is far smaller than L_{PM}. Therefore, the following is derived

$$\left(R_{+YU} \, / / \, R_{+YL} + R_{+XU} \, / / \, R_{+XL} \right) \ll R_{PM} \quad (15)$$

By combing Eq. (7), Eq. (8), Eq. (10)-Eq. (13) and Eq. (15), the simplified PM fluxes that are generated by the "1U" PM and flow through the "+Y" upper and lower air gaps are given by

$$\Phi_{+YU}^{1U} = B_r A_{PM} \frac{L_0 + \theta_X r}{2 L_0} \quad (16)$$

$$\Phi_{+YL}^{1U} = B_r A_{PM} \frac{L_0 - \theta_X r}{2 L_0} \quad (17)$$

According to the actuator's symmetry and noticing that the total PM fluxes flowing through the +Y air gaps are the superposition of the PM fluxes generated by the 1U, 1L, 4U, and 4L permanent magnets, we determine the total PM fluxes following through the "+Y" upper and lower air gaps

$$\Phi_{+YU}^{PM} = 4 \Phi_{+YU}^{1U} = 2 B_r A_{PM} \frac{L_0 + \theta_X r}{L_0} \quad (18)$$

$$\Phi_{+YL}^{PM} = 4 \Phi_{+YL}^{1U} = 2 B_r A_{PM} \frac{L_0 - \theta_X r}{L_0} \quad (19)$$

Dividing Eq. (18) and Eq. (19) by the air gap pole area A_g gives the net PM flux densities in the "+Y" upper and lower air gaps respectively

$$B_{+YU}^{PM} = \frac{2 B_r A_{PM}}{A_g} \cdot \frac{L_0 + \theta_X r}{L_0} \quad (20)$$

$$B_{+YL}^{PM} = \frac{2 B_r A_{PM}}{A_g} \cdot \frac{L_0 - \theta_X r}{L_0} \quad (21)$$

Once again utilizing the actuator's symmetry, we can easily determine the net PM flux densities in the "–Y" upper and lower air gaps as

$$B_{-YL}^{PM} = B_{+YU}^{PM} = \frac{2 B_r A_{PM}}{A_g} \cdot \frac{L_0 + \theta_X r}{L_0} \quad (22)$$

$$B_{-YU}^{PM} = B_{+YL}^{PM} = \frac{2 B_r A_{PM}}{A_g} \cdot \frac{L_0 - \theta_X r}{L_0} \quad (23)$$

Therefore, the total bias PM flux density in each air gap is a linear function of the rotation angle according to Eq. (22) and Eq. (23).

Solving the equivalent magnetic circuit model shown by Fig. 7 and noticing that $R_{+YU} + R_{+YL}$ is equal to $R_{-YU} +$

R_{-YL}, we obtain the identical coil flux flowing through the "+Y" and "−Y" air gaps

$$\Phi_{+YU}^{Coil} = \Phi_{+YL}^{Coil} = \Phi_{-YU}^{Coil} = \Phi_{-YL}^{Coil} = \frac{\Psi_{+Y}}{R_{+YU} + R_{+YL}} = \frac{N\mu_0 A_g}{2L_0} I_Y \quad (24)$$

Dividing the coil flux by the air gap pole area yields the identical coil flux density in the "+Y" and "−Y" air gaps

$$B_{+YU}^{Coil} = B_{+YL}^{Coil} = B_{-YU}^{Coil} = B_{-YL}^{Coil} = \frac{N\mu_0}{2L_0} I_Y \quad (25)$$

The reluctances R_{+YU} and R_{+YL} vary with the armature position, but $R_{+YU} + R_{+YL}$ is a constant independent of the change of the armature position. From Eq. (25), one can easily obtain that the coil flux density is a linear function of the driving current, without being affected by the armature position.

3.2. Actuating Torque Modeling

To simplify analysis, flux leakage is neglected in the previous analysis. However, flux leakage, especially the PM flux leakage, exists in the actuator and affects the computation accuracy of the actuator's torque output greatly. Therefore, both the coil flux and PM flux leakages must be involved in the actuator's torque computation to improve modeling accuracy. In order to take the flux leakage of the actuator into account, the PM flux leakage factor β_{PM} and the coil flux leakage factor β_{Coil} are defined to modify the obtained ideal PM and coil fluxes. β_{PM} and β_{Coil} are given by

$$\beta_{PM} = \frac{\overline{\Phi}_{+Y}^{PM}}{\Phi_{+Y}^{PM}} \quad (26)$$

$$\beta_{Coil} = \frac{\overline{\Phi}_{+Y}^{Coil}}{\Phi_{+Y}^{Coil}} \quad (27)$$

where $\overline{\Phi}_{+Y}^{PM}$ and $\overline{\Phi}_{+Y}^{Coil}$ respectively denote the real total PM and coil fluxes flowing through the "+Y" air gaps and can be obtained via 3D finite element simulations, Φ_{+Y}^{PM} and Φ_{+Y}^{Coil} respectively denote the ideal total PM and coil fluxes flowing through the "+Y" air gaps and can be calculated as

$$\Phi_{+Y}^{PM} = \Phi_{+YU}^{PM} + \Phi_{+LU}^{PM} = 4B_r A_{PM} \quad (28)$$

$$\Phi_{+Y}^{Coil} = \Phi_{+YU}^{Coil} = \frac{N\mu_0 A_g}{2L_0} I_Y \quad (29)$$

It can be seen from Fig. 6 that the total flux density in each air gap is the superposition of the PM flux density and coil flux density. Combing Eq. (18)-Eq. (29) and noticing the directions of the PM and coil fluxes, we obtain the real total flux densities in the "+Y" and "−Y"

air gaps as follows:

$$B_{+YU} = B_{-YL} = \beta_{PM} B_{+YU}^{PM} + \beta_{Coil} B_{+YU}^{Coil}$$

$$= \frac{2\beta_{PM} B_r A_{PM}}{A_g} \cdot \frac{L_0 + \theta_X r}{L_0} + \frac{\beta_{Coil} N\mu_0}{2L_0} I_Y \quad (30)$$

$$B_{+YL} = B_{-YU} = \beta_{PM} B_{+YL}^{PM} - \beta_{Coil} B_{+YL}^{Coil}$$

$$= \frac{2\beta_{PM} B_r A_{PM}}{A_g} \cdot \frac{L_0 - \theta_X r}{L_0} - \frac{\beta_{Coil} N\mu_0}{2L_0} I_Y \quad (31)$$

where B_{+YU} is the real total flux density in the "+Y" upper air gap, B_{-YL} is the real total flux density in the "−Y" lower air gap, and so on.

Considering the contributions of the fluxes in the upper and lower gaps, we derive the resultant electromagnetic forces generated by the total fluxes in the "+Y" and "−Y" air gaps

$$F_{+Y} = F_{-Y} = A_g \frac{\left(B_{+YU}\right)^2 - \left(B_{+YL}\right)^2}{2\mu_0}$$

$$= \frac{8\beta_{PM}^2 B_r^2 A_{PM}^2 r}{A_g L_0 \mu_0} \theta_X + \frac{2\beta_{PM} B_r A_{PM} N \beta_{Coil}}{L_0} I_Y \quad (32)$$

where F_{+Y} and F_{-Y} denote the resultant electromagnetic forces generated by the fluxes in the "+Y" upper and lower air gaps and "−Y" upper and lower air gaps, respectively.

Note that F_{+Y} and F_{-Y} are equal and opposite. Hence, the net force acting on the armature is null and a torque pointing to positive X-direction is generated on the armature. Multiplying F_{+Y} by $2r$ gives the actuating torque output

$$T_X = 2F_{+Y} r = K_\theta \theta_X + K_I I_Y \quad (33)$$

where

$$K_\theta = \frac{16\beta_{PM}^2 B_r^2 A_{PM}^2 r^2}{A_g L_0 \mu_0} \quad (34)$$

$$K_I = \frac{4\beta_{PM}\beta_{Coil} B_r A_{PM} N r}{L_0} \quad (35)$$

As K_θ and K_I are constants, the actuating torque output T_X is a linear function of both the rotation angle θ_X and driving current I_Y. The other one actuating torque T_Y which controls the steering motion θ_Y can be derived based on the actuator's symmetry

$$T_Y = K_\theta \theta_Y + K_I I_X \quad (36)$$

3.3. Flux Leakage Analysis

In this paper, both the PM flux and coil flux leakages are taken into consideration via 3D finite element simu-

lations and curve fitting method to improve computation accuracy. Fig. 8 shows the finite element analysis model of the actuator in this paper. To simplify the simulation, some design parameters of the actuator have been determined in advance according to the requirements of our FSM. Because of fabrication problem, each curved permanent magnet is replaced by the combination of two cube permanent magnets in the simulation model. The length of the cross armature, D_O (refer to Fig. 3), is mainly determined by the flexure support system (refer to Fig. 1(c)) and is designed to be 25 mm. The initial air gap length L_0 is designed to be 0.3 mm to meet the FSM's angular range requirement of ±10 mrad. The height of the empty region within the core which is left for winding the coils is mainly controlled by the length of the coil windings and is designed to be 25 mm. The cores, armature and flux directing steels are assigned with the material of 'iron'. The coils are assigned with the material of 'copper'. The solving domain is assigned with the material of 'vacuum'. The remanence of the chosen neodymium-iron-boron permanent magnet is 1.2 T and the length of each permanent magnet in Fig. 8 is designed to be 5 mm to provide adequate bias MMF. The cross sectional area of the armature is set to be twice that of the PM. Hence, only A_g and A_{PM} vary in the simulation model. The current carrying face of each coil is used to assign current source to the coil. Ansoft Maxwell's meshing algorithm is adaptive. It refines the mesh before the output variable converges sufficiently. To achieve high computation accuracy, a fine initial mesh is assigned to the finite element model. Fig. 9 shows the initial mesh.

The air gap pole area A_g partly determines the maximum torque output of the actuator, which must meet the torque requirement of the FSM. By using 3D finite element simulation, the design scope of A_g is set to be 5 mm^2 < A_g < 20 mm^2. The ratio of A_{PM} to A_g determines the bias flux density. From Eq. (22) and Eq. (23), we know that a larger A_{PM}/A_g results in a larger bias flux density. Hence, a larger actuating torque is generated. However, too large A_{PM}/A_g is not allowed to avoid the flux saturation inside the core. Again using finite element simulation, we set 0.7 < A_{PM}/A_g < 1.3.

The PM flux leakage factor β_{PM} is calculated directly by using Eq. (26) and Eq. (28). The real total PM flux $\overline{\Phi}_{+Y}^{PM}$ is determined by

$$\overline{\Phi}_{+Y}^{PM} = \int_{S_{+YU}} \overline{B}_{+YU}^{PM} + \int_{S_{+YL}} \overline{B}_{+YL}^{PM} \tag{37}$$

where S_{+YU} and S_{+YL} respectively indicate the middle surfaces of the "+Y" upper and lower air gaps, $\overline{B}_{+YU}^{PM}$ and $\overline{B}_{+YL}^{PM}$ respectively denote the real PM flux densities of the
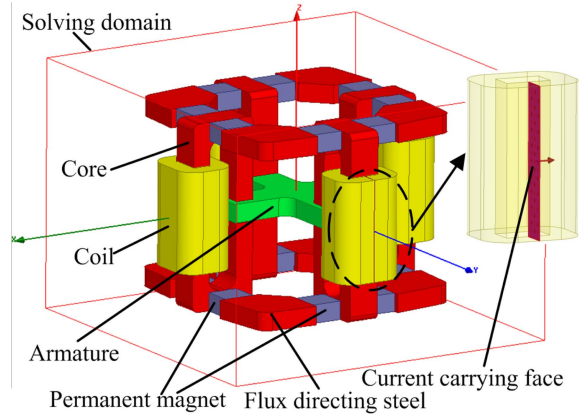

Fig. 8. (Color online) Magnetic finite element analysis model of the actuator in this paper.

surfaces S_{+YU} and S_{+YL} and can be obtained via 3D finite element simulation. After obtaining the discrete β_{PM} via simulation, curve fitting method is then used to approximate β_{PM} as a function of A_g. To decrease simulation time, the four coils are removed from the finite element model shown by Fig. 8. Only the components related to the PM flux magnetic circuit are taken into account when
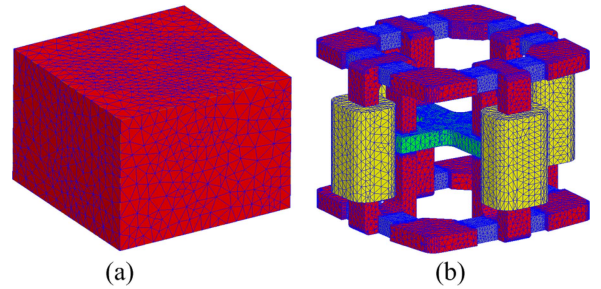

Fig. 9. (Color online) Initial mesh of the finite element model. (a) Initial mesh of the solving domain, (b) initial mesh of the actuator.
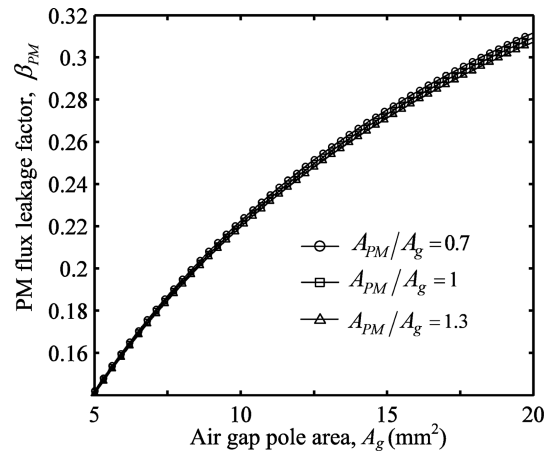

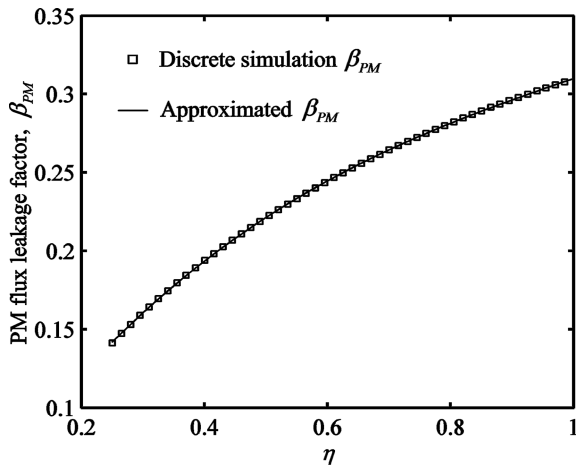**Fig. 10.** Simulation results of the PM flux leakage factor.

Fig. 11. Approximated PM flux leakage factor obtained via curve fitting method.

Fig. 12. Simulation results of the coil flux leakage factor.

calculating the PM flux leakage factor β_{PM}.

Using Ansoft Maxwell's parametric simulation, we obtain the discrete PM flux leakage factor β_{PM} as Fig. 10 shows. It is evident that β_{PM} is an increasing function of A_g. The ratio of A_{PM} to A_g has little effect on the PM flux leakage. Due to the long PM flux path and small air gap pole area, most of the PM flux leaks out into air ($\beta_{PM} < 0.5$). However, it is still easy to achieve a high bias flux density without using too big PMs because there are four PM MMF sources for one air gap.

As β_{PM} is not affected by A_{PM}/A_g, we use the discrete simulation β_{PM} obtained with $A_{PM}/A_g = 1$ to approximate β_{PM} as a function of A_g. To simplify analysis, variable η defined by $\eta = A_g/A_{max}$ where $A_{max} = 20$ mm^2 is introduced in the analysis. In this paper, cubic polynomial is used to fit the discrete simulation β_{PM} and the approximated β_{PM} as a cubic polynomial function of η is obtained as

$$\beta_{PM}(\eta) = 0.13062\eta^3 - 0.41613\eta^2 + 0.57295\eta + 0.02241 \quad (38)$$

Fig. 11 plots the curve of $\beta_{PM}(\eta)$, along with the discrete simulation β_{PM}. It can be seen that the discrete simulation β_{PM} is in a good agreement with the approximated $\beta_{PM}(\eta)$ obtained via curve fitting method.

The coil flux leakage factor β_{Coil} is calculated by using Eq. (27) and Eq. (29), directly. The real coil flux $\overline{\Phi}_{+Y}^{Coil}$ is given by

$$\overline{\Phi}_{+Y}^{Coil} = \int_{S_{+YU}} \overline{B}_{+YU}^{Coil} = \int_{S_{+YL}} \overline{B}_{+YL}^{Coil} \quad (39)$$

where $\overline{B}_{+YU}^{Coil}$ and $\overline{B}_{+YL}^{Coil}$ respectively denote the real coil flux densities of the surfaces S_{+YU} and S_{+YL} and can be obtained via 3D finite element simulation.

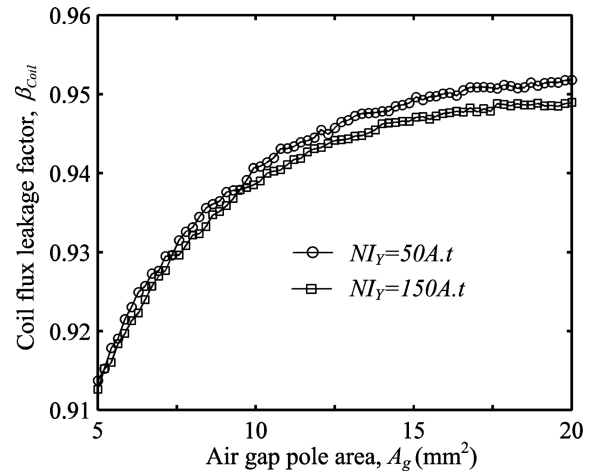As the coil fluxes are not affected by the PMs and the actuator is symmetric, only the armature and one of the four coils along with its core are involved in the 3D finite element simulation model used to calculate the coil flux leakage factor β_{Coil}. To examine whether the coil MMF affects β_{Coil}, the coil MMF also varies in the simulation model apart from the air gap pole face area A_g.

Fig. 12 shows the simulation results of β_{Coil}. It can be seen that most of the coil flux flows inside the core ($\beta_{Coil} > 0.9$) and the coil MMF almost has no effect on β_{Coil}. The coil flux leakage factor β_{Coil} varies with A_g, but not significantly ($0.91 < \beta_{Coil} < 0.96$). Hence, it is preferable to determine β_{Coil} by referring to Fig. 12 rather than by approximating it with curve fitting method when designing the actuator.

4. Validation and Analysis with Finite Element Simulation

To validate the concept design and magnetic analysis, a testing actuator with $A_{PM} = A_g = 15$ mm^2 is designed. Then, a large number of simulations with varying coil MMF and rotation angle are carried out to examine the testing actuator's characteristics based on the magnetic finite element model shown by Fig. 8. Using Ansoft Maxwell's parametric simulation function, we can conveniently achieve these simulations without too much human intervention.

To show the effectiveness that the concept design in this paper can eliminate the additional axial force, a sAFSM-type actuator that has the same dimensions as the testing actuator is also designed. The additional axial forces of the two actuators are calculated via 3D finite element simulations.

The additional axial force of the sAFSM-type actuator is shown in Fig. 13. It can be seen that the additional axial force of the sAFSM-type actuator varies with the
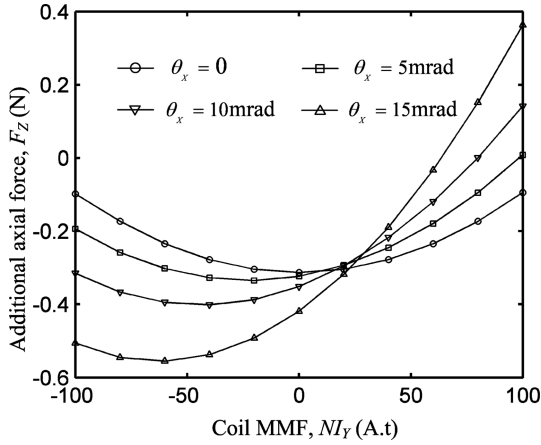
Fig. 13. Additional axial force of the sAFSM-type actuator.

Fig. 15. Simulation and calculated torques versus the coil MMF.

driving current, indicating the potential risk of resonance.

Fig. 14 shows the additional axial force of the testing actuator in this paper. It can be seen that the simulation additional axial force of the testing actuator is on the order of millinewton and is a constant independent of the driving current. In fact, the simulation additional axial force of the testing actuator is mainly caused by the finite element simulation error.

Substituting $\eta = 0.75$ ($A_g = 15$ mm^2) into Eq. (38) gives the PM flux leakage factor β_{PM} of the testing actuator. By referring to Fig. 12, the coil flux leakage factor β_{Coil} of the testing actuator is also obtained. Therefore, all the unknown parameters in Eq. (34) and Eq. (35) are determined. Then, the analytical torque output of the testing actuator as a function of the rotation angle and coil MMF is obtained. In the following analysis, finite element simulation will be used to examine the effectiveness of the analytical torque output model.

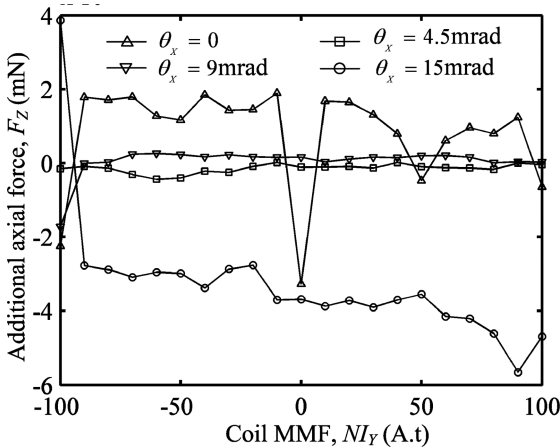Fig. 15 plots the simulation result of the testing actuator's

torque output versus the coil MMF when the armature is centered, along with the calculated result from the analytical model. The finite element simulation result confirms that the actuating torque is a linear function of the driving current. The analytical actuator model has high accuracy, especially in small rotation angle range. Compared with the analytical model of the sAFSM actuator in Ref. [12], the analytical model of the actuator in this paper is far more accurate as both the PM flux and coil flux leakages are involved in the analysis and modeled properly.

As Fig. 16 shows, the testing actuator's torque output is nearly linear with the rotation angle, especially when the rotation angle is small. It is obvious in Fig. 16 that the testing actuator's torque output is nearly a linear function of the rotation angle in the angular range of ± 10 mrad, which meets the angular requirement of our FSM. However, nonlinearity is visible in the simulation curve, especially in large rotation angle range. This nonlinearity
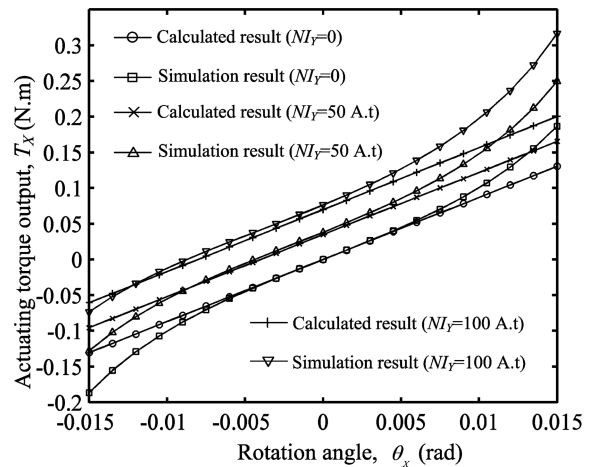

Fig. 14. Additional axial force of the testing actuator in this paper.

Fig. 16. Simulation and calculated torques versus the rotation angle.

is mainly caused by the not truly linear relationship between the air gap reluctance and rotation angle. The relative error of the calculated torque increases with the rotation angle as the nonlinearity is more obvious in large rotation angle range.

5. Conclusion

In this paper, a new two-axis rotary electromagnetic actuator which works on normal stress is designed to drive our FSM. The actuator is with a compact structure and has high force density similar to a solenoid. The 3D finite element simulation results confirm that there is no additional axial force generated on the armature and the actuator's torque output is nearly a linear function of both the driving current and rotation angle, indicating that the actuator is ideal for FSM. As there are four permanent magnet magnetomotive force sources for one air gap, which benefits from the "top-bottom" arrangement of the permanent magnets, it is easy to achieve a high bias flux density in each air gap without the need of big permanent magnets. In addition, the actuator is with a new cross topology armature which tends to decreases the armature's moment of inertia about the working axis, and thereby a higher bandwidth of our FSM can be achieved. For the analytical magnetic analysis and actuating torque modeling, both the permanent magnet flux and coil flux leakages must be taken into consideration to achieve an accurate analytical actuator model. Our future work will focus on the actuator's optimal design, manufacturing a prototype of the actuator, and demonstrating our design with experiment. Then, the real actuator and the other components of our FSM will be assembled together to test control algorithm and improve the FSM's performance.

Acknowledgements

References

[1] G. C. Loney, Proc. SPIE **1454**, 198 (1991).
[2] K. Aoki, Y. Yanagita, H. Kuroda, and K. Shiratama, Proc. SPIE **5160**, 495 (2004).
[3] X. Wu, S. Chen, B. Shi, W. Chen, and X. Xiong, Opt. Eng. **50**, 023002 (2011).
[4] Y. Lu, D. Fan, and Z. Zhang, Optik **124**, 2443 (2013).
[5] S. Woody, and S. Smith, Mechatronics **16**, 389 (2006).
[6] S. Bing, R. Weibin, G. Bin, R. Changhai, and S. Lining, Smart Mater. Struct. **17**, 025032 (2008).
[7] X. Lu, Ph.D. Thesis, Massachusetts Institute of Technology, America (2005).
[8] D. Wu, X. Xie, and S. Zhou, IEEE Trans. Magn. **46**, 1007 (2010).
[9] R. C. Montesanti, Ph.D. Thesis, Massachusetts Institute of Technology, America (2005).
[10] D. P. Cuff, M.S. Thesis, Massachusetts Institute of Technology, America (2006).
[11] R. H. Maskrey and W. J. Thayer, Trans. ASME, J. Dynamic Systems, Measurement Control **100**, 110 (1978).
[12] D. J. Kluk, M. T. Boulet, and D. L. Trumper, Mechatronics **22**, 257 (2009).
[13] M. T. Boulet, M.S. Thesis, Massachusetts Institute of Technology, America (2008).